batteries

MDPI

Article

State of Charge Estimation of Lithium-ion Batteries Based on Online OCV Curve Construction

Xuemei Wang *, Ruiyun Gong, Zhao Yang and Longyun Kang

School of Electric Power, South China University of Technology, Guangzhou 510640, China; lykang@scut.edu.cn (L.K.)
* Correspondence: epxmwang@scut.edu.cn

Abstract: The open-circuit voltage (OCV) curve has a significant influence on the accuracy of the state of charge (SOC) estimation based on equivalent circuit models (ECMs). However, OCV curves are tested through offline experiments and are hard to be very accurate because they constantly change with the test method's ambient temperature and aging status. Recently, researchers have attempted to improve the accuracy of OCV curves by increasing the volume of sample data or updating/reconstructing the curve combined with practical operation data. Still, prior offline tests are essential, and experimental errors inevitably exist. Consequently, a SOC estimation method without any offline OCV tests might be an efficient route to improve the accuracy of SOC. According to this idea, this paper presents a novel method for SOC estimation, which is based on online OCV curve construction. Meanwhile, a stepwise multi-timescale parameter identification algorithm is designed to improve the interpretability and precision of the estimated ECM parameters. The results demonstrate that the maximum SOC estimation error is only 0.05% at 25 °C, indicating good robustness under various ambient temperatures and operational conditions.

Keywords: open-circuit voltage; state of charge; equivalent circuit model; parameter identification

check for updates

Citation: Wang, X.; Gong, R.; Yang, Z.; Kang, L. State of Charge Estimation of Lithium-ion Batteries Based on Online OCV Curve Construction. *Batteries* **2024**, *10*, 208. https://doi.org/10.3390/batteries10060208

Academic Editor: Vilayanur Viswanathan

Received: 6 May 2024
Revised: 4 June 2024
Accepted: 14 June 2024
Published: 16 June 2024

Copyright: © 2024 by the authors. Licensee MDPI, Basel, Switzerland. This article is an open access article distributed under the terms and conditions of the Creative Commons Attribution (CC BY) license (https://creativecommons.org/licenses/by/4.0/).

1. Introduction

Lithium-ion batteries (LiBs) are widely used in electric vehicles (EVs) and energy storage systems due to their high energy density, long life cycle, low self-discharge rate, and so on [1,2]. The battery performance is monitored by a battery management system (BMS), in which the SOC is one of the most important status indicators [3]. Currently, commonly used SOC estimation algorithms include the OCV method, ampere–hour integration method, model-based method, and data-driven method [4–6], among which the ECM-based method is widely used in EVs due to its comparatively high accuracy and low computational effort [7,8].

Various Kalman filtering (KF) algorithms, such as extended Kalman filter (EKF), adaptive Kalman filter (AKF), and unscented Kalman filter (UKF), are often used in ECM-based SOC estimation because of their good estimation accuracy. In the OCV curve (also known as the "OCV–SOC curve"), the relationship between OCV and SOC is very crucial for SOC estimation by KF algorithms [9–11]. For instance, if the OCV error is greater than 10 mV, the error of the OCV-based SOC estimation may be as high as 5% [12]. The battery OCV is defined as the potential difference between the positive and negative electrodes when the electrode potentials are at equilibrium. The electrode equilibrium potential is the potential difference between the electrode and electrolyte when the electrode is in a state of electrochemical equilibrium. Thus, OCV curves are usually obtained through offline OCV tests, including the incremental OCV test and the low-current OCV test, with the former considered more popular because of its reliable accuracy. However, there are three deficiencies in obtaining the OCV curves through offline OCV tests. First, OCV tests are quite time-consuming. It usually takes 2–3 h of relaxation to obtain accurate OCV, so a test

including full charging and discharging cycle will take 3–5 days [13]. Second, OCV tests are typically performed at every 10% SOC interval, and the obtained data are raw and not completely credible [14,15]. Third, batteries operate over a wide range of temperatures, and OCV curves inevitably vary with changes in ambient temperature and state of health (SOH) [16,17]. Therefore, multiple repeated OCV tests under different temperatures and SOHs are required to ensure the accuracy of SOC estimation. At present, the solution to the above problems mainly revolves around decreasing the OCV curve measurement time [18–21]. Pei et al. provided a linear regression technique to rapidly predict OCV with an error lower than 1 mV by 20 min relaxation time [18]. Zhou et al. proposed an OCV prediction method obtained from a first-order RC circuit model without the entire voltage relaxation information, avoiding mathematical fitting and decreasing the OCV measurement time to a few minutes [19]. Ko et al. used a Gaussian process regression model to estimate OCV and SOH with only 30 s relaxation voltage [20]. Yang et al. actively decreased polarization voltage during OCV tests by superposing a current excitation, and the relaxation time was also effectively shortened [21].

Although the above studies have partly solved the problems of long measurement time of OCV tests, the OCV–SOC relationships obtained under fixed temperatures and aging conditions inevitably have errors and poor robustness due to variable environments and SOHs in practical operation [22]. To tackle these issues, some studies concentrate on partially/fully updating or reconstructing the OCV curve based on the practical operation data [13,22,23]. Chen et al. proposed a method where SOC could be estimated based on the OCV curve reconstructed partially, whose data were extracted from the accumulated data of EV practical operations rather than experiments. However, historical experiment data were still concentrated, and the maximum error of SOC estimation was close to 3% [24]. Wang et al. extracted the OCV–SOC relationship from low-current (0~0.002 C) operational data stored in the cloud in the range of 40–80% SOC and then spliced with the experimental OCV curve of SOC < 40% and SOC > 80%. So, the intermediate phase transition part of the OCV curve was updated [23]. Xiong et al. proposed a method that extracted the OCV–SOC relationship from existing charge/discharge data using a H∞ filter, and the OCV–SOC relationship used in the nth charge/discharge process was from the $(n-1)$th charge/discharge process [13]. However, the establishment of the OCV–SOC relationship requires a complete charge/discharge process, which does not easily satisfy the real-time update requirements of EVs. Zhang et al. [22] employed an ampere–hour integration method to calculate the SOC first. When the variation in battery capacity Q exceeded the pre-set threshold ($\Delta Q > Q_{\text{threshold}}$), an EKF algorithm was used to partially reconstruct the OCV curves. Although the experimental OCV curves were not required, the algorithm was fundamentally an open-loop empirical correction. As a result, the maximum SOC estimation errors were still as high as 1%.

The above studies have solved the robustness issue of the OCV curve to some extent, but there are still two deficiencies: (1) For offline experiments, the OCV curve is still hard to measure precisely because of the inevitable SOC estimation errors [13,22]. Consequently, a SOC estimation method without any offline OCV tests might be an efficient approach; (2) OCV curves are different for various types of batteries, different temperatures, and aging status. It would be a feasible way to estimate SOC accurately if the OCV curve is updated when a battery is working [24]. Based on these ideas, this paper presents a SOC estimation algorithm based on online OCV curve construction, which has not been studied yet. The main contributions are as follows:

1. The OCV curve is entirely constructed online without any offline tests, and the experimental cost is reduced dramatically. With the proposed method, the OCV curve is constructed in real time, and the problem of long experimental time and finite data generated by offline OCV tests is avoided. Furthermore, since offline OCV experiments are no longer required, in theory, the algorithm can be applied under different temperatures, SOHs, and working conditions; thus, the robustness of SOC estimation will be increased significantly.

2. A stepwise parameter identification algorithm, namely fixed-memory recursive least squares–extended Kalman filtering–Kalman filtering (FMRLS-EKF-KF), is proposed. Different timescales and algorithms associated with different electrochemical processes of LiBs are used to identify the parameters to avoid their cross-interference. As a result, the parameters identified in this paper have explicable and explainable kinetic significance compared to existing identification algorithms.
3. Excellent SOC estimation accuracy is achieved. This method reduces the overall SOC estimation errors by about 30–50 times compared with traditional methods based on offline OCV tests, and the maximum error is only 0.005% at 25 °C. Meanwhile, it maintains high accuracy under various ambient temperatures and operating conditions.

This paper is structured as follows: Section 2 briefly introduces the ECM model of LiBs, and the FMRLS-EKF-KF stepwise parameter identification algorithm is proposed. Section 3 introduces the EKF-KF algorithm in detail. Section 4 elaborates on the OCV curve online construction method and the SOC estimation algorithm. Finally, the results and conclusions are presented in Section 5. All notations are provided in Table 1.

Table 1. Basic notations used in the article.

Notations	Definition
U_{OCV}	Battery open-circuit voltage
R_0	Battery internal resistance
R_j (j = 1, 2)	Equivalent polarization resistance of the battery
C_j (j = 1, 2)	Equivalent polarization capacitance of the battery
u_0	Terminal voltage of R_0
u_j (j = 1, 2)	Terminal voltage of R_jC_j network
u_t	Battery terminal voltage
i_t	Battery terminal current
u_{SD}	Terminal voltage of the slow dynamic part
u_{FD}	Terminal voltage of the fast dynamic part
T_{s}	The sampling period of BMS
ΔT	The time interval for each identification period of R_2C_2
i_2	The current flows through R_2
SOC	Battery state of charge
f (SOC)	The polynomial model of OCV–SOC relationship
a_j (j = 1, 2, . . ., n)	Polynomial coefficients
$\boldsymbol{\Phi}_k$	Data vector at the kth moment
$\boldsymbol{\theta}_k$	Parameter vector at the kth moment
y_k	Output vector at the kth moment
λ	The forgetting factor of the FFRLS algorithm
Q_{a}	The maximum available capacity of the battery
η	Coulomb efficiency
$\boldsymbol{X}_k$	State variable at the kth moment
$\boldsymbol{O}_k$	Output variable at the kth moment
$\boldsymbol{A}_k$, $\boldsymbol{B}_k$, $\boldsymbol{C}_k$, $\boldsymbol{D}_k$	Coefficient matrices of the state equation and output equation

2. Overall Algorithm Structure of SOC Estimation

There are many kinds of ECMs for LiBs, among which the second-order RC model is one of the most widely used because it provides a good compromise between simplicity and accuracy. Figure 1 is the second-order ECM model, where the voltage source U_{OCV} represents the battery's OCV; u_{t} and i_{t} are the terminal voltage and current, respectively; R_0 denotes the ohmic resistance; R_1 and C_1 represent the equivalent resistance and capacitance of the charge transfer process; and R_2 and C_2 represent the equivalent resistance and capacitance of the diffusion process. The ECM model may be divided into two modules of fast dynamics (FD) and slow dynamics (SD) based on the multi-timescale characteristics of LiBs, where U_{OCV}, R_2, C_2 form the SD part and R_0, R_1, and C_1 constitute the FD part [25].

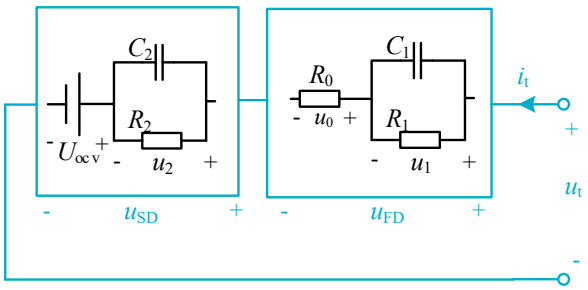

Figure 1. Second−order RC ECM [25].

The overall structure of the proposed SOC estimation algorithm is shown in Figure 2, which includes three parts: multi-timescale parameters identification, SOC estimation, and online OCV curve construction. The most notable features of this algorithm are as follows: (1) The OCV–SOC relationship for SOC estimation comes from online modeling instead of offline experimental measurements. (2) The ECM parameters are identified by the stepwise multi-timescale method FMRLS-EKF-KF.

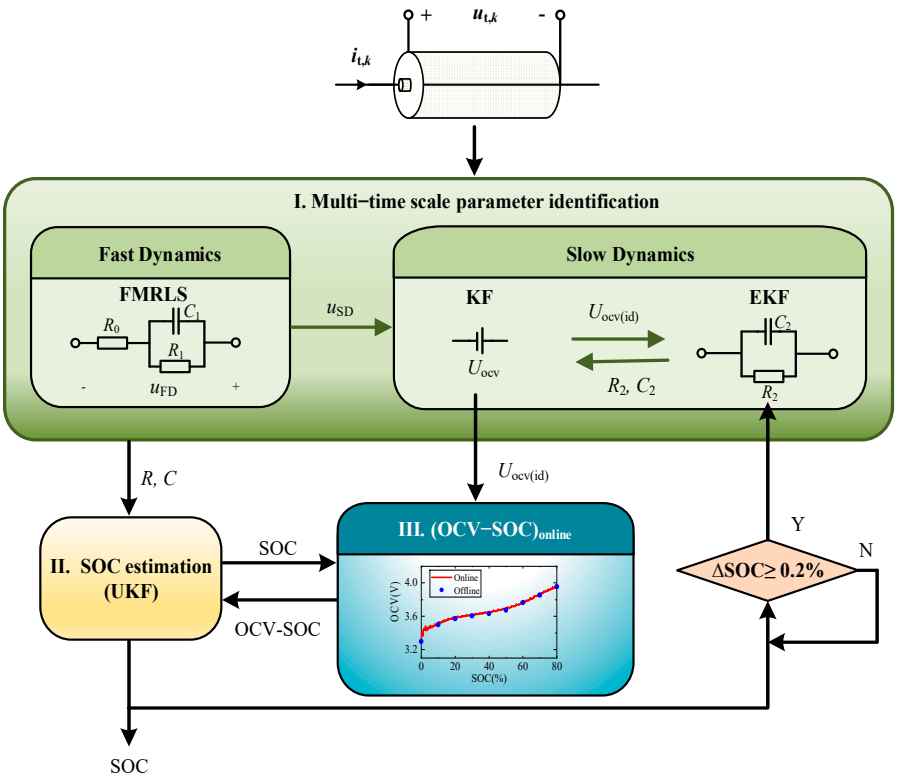

Figure 2. The overall algorithm structure SOC estimation.

The process of the kth algorithm cycle is as following steps: Step (1): R_0, R_1, C_1, R_2, C_2, and U_{OCV} are estimated using the FMRLS-EKF-KF algorithm proposed. Step (2): According to the OCV–SOC relationship, which is modeled during the last cycle, here named $f(\text{SOC})_{k-1}$ first, SOC_k is estimated using the UKF algorithm. Step (3): The U_{OCV} value determined from step 1 and the SOC_k estimated at step 2 are fitted using the forgetting factor recursive least-square (FFRLS) method to obtain the new OCV–SOC relationship, that is, $f(\text{SOC})_k$. The detailed algorithm will be introduced in the next two sections.

3. Multi-Timescale Parameter Identification Algorithm

Accurate circuit parameters are the basis of SOC estimation based on ECM. A stepwise FMRLS-FEKF identification algorithm considering the multi-timescale characteristics of

LiBs was proposed in our previous studies [25]. Although the results show that the terminal voltage errors are very small (<1 mV at 25 °C), the identified SD parameters lack explainable kinetic significance.

In this paper, a modified multi-timescale identification algorithm, namely FMRLS-EKF-KF, is proposed, where the FMRLS and EKF-KF algorithms are used to identify parameters of the FD and SD parts, respectively. The FMRLS algorithm has been previously introduced in detail [25], and will not be presented again in this paper. For the SD part, the EKF-KF algorithm is proposed to avoid cross-interference between U_{OCV} and R_2C_2. The flowchart of EKF-KF is illustrated in Figure 3, which includes two Kalman filtering algorithms: KF is for slow U_{OCV} identification and EKF is for ultra-slow R_2C_2 identification. In order to maintain consistency with SOC estimation, the identification period of U_{OCV} should be consistent with the sampling time of BMS. By contrast, R_2C_2 is identified when $|\Delta SOC| \geq 0.2\%$ (the motivation will be explained later). In Figure 3, $\hat{U}_{OCV}^{-}$, $\hat{R}_2^{-}$, and $\hat{C}_2^{-}$ are the prediction parameters, while $\hat{U}_{OCV}$, $\hat{R}_2$, and $\hat{C}_2$ are the correction parameters.

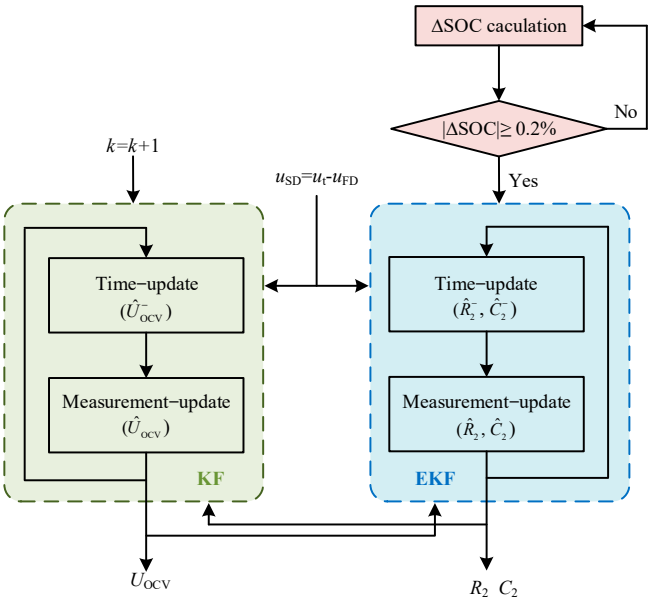

Figure 3. EKF−KF algorithm flowchart of the SD part.

3.1. U_{OCV} Identification Based on KF

U_{OCV} is identified using the KF algorithm, whose algorithm process can be found in [26]. Considering practical application, U_{OCV} varies very little per sampling period, so its discretized state equation and output equation can be expressed as follows:

$$\begin{cases} U_{OCV,k+1} = U_{OCV,k} \\ u_{SD,k} = U_{OCV,k} + u_{2,k} \end{cases} \tag{1}$$

where k is the discretization time index, and u_2 is the voltage of R_2C_2, which can be obtained from the circuit model of Figure 1 as follows:

$$u_{2,k+1} = e^{-\frac{T_s}{R_{2,k}C_{2,k}}} \cdot u_{2,k} + R_{2,k}\left(1 - e^{-\frac{T_s}{R_{2,k}C_{2,k}}}\right) \cdot i_{t,k} \tag{2}$$

where T_s is the sampling period of BMS. The identification algorithm of R_2C_2 will be introduced in the next section. The reference value of u_{SD} is calculated as $u_{SD} = u_t - u_{FD}$, where u_{FD} is the voltage of the FD part and is obtained using the FMRLS algorithm. Since the typical sampling period T_s of BMS systems is 1 s, 1 s is also adopted as the algorithm period in this paper.

3.2. R_2C_2 Identification Based on EKF

R_2 and C_2 are identified using the EKF, whose algorithm process can be found in [27]. Dividing the two sides of (2) by R_2, i_2 (the current flows through R_2) can be expressed as:

$$i_{2,j+1} = e^{-\frac{\Delta T_j}{R_{2,j}C_{2,j}}} \cdot i_{2,j} + \left(1 - e^{-\frac{\Delta T_j}{R_{2,j}C_{2,j}}}\right) \cdot i_{t,j} \tag{3}$$

where ΔT represents the time interval for each identification period of R_2C_2, which is performed when $|\Delta\text{SOC}| \geq 0.2\%$. As is well known, the time constant of R_2C_2 is around tens or hundreds of seconds and changes more gradually than OCV because it represents the LiBs' diffusion process in the battery electrodes. If a short sampling period is utilized, it may result in data saturation or cross-interference with OCV and eventually result in inaccurate parameter identifications [28]. What needs illustration is that $|\Delta\text{SOC}| \geq 0.2\%$ is a tradeoff between compute time and the accuracy of the simulations. If $|\Delta\text{SOC}|$ is too large, the identification accuracy is low; conversely, if $|\Delta\text{SOC}|$ is too small, the compute time taken is long. Since R_2 and C_2 all vary very slowly, it is assumed that

$$\begin{cases} R_{2,j+1} = R_{2,j} \\ C_{2,j+1} = C_{2,j} \end{cases} \tag{4}$$

where j is the discretization index. The discretized state equation and the output equation of R_2C_2 identification algorithms can be expressed as follows:

$$\begin{bmatrix} i_{2,j+1} \\ R_{2,j+1} \\ C_{2,j+1} \end{bmatrix} = \begin{bmatrix} e^{-\frac{\Delta T_j}{R_{2,j}C_{2,j}}} & 0 & 0 \\ 0 & 1 & 0 \\ 0 & 0 & 1 \end{bmatrix} \cdot \begin{bmatrix} i_{2,j} \\ R_{2,j} \\ C_{2,j} \end{bmatrix} + \begin{bmatrix} 1 - e^{-\frac{\Delta T_j}{R_{2,j}C_{2,j}}} \\ 0 \\ 0 \end{bmatrix} \cdot i_{t,j} \tag{5}$$

$$u_{SD,j} = i_{2,j}R_{2,j} + U_{\text{OCV},\,j} \tag{6}$$

where i_2, R_2, and C_2 are state variables, and u_{SD} is the output variable.

4. SOC Estimation Method Based on Online Constructed OCV Curves

4.1. Online OCV Curve Construction by FFRLS

One of the popular modeling methods of the OCV–SOC relationship is the polynomial model, which has good fitting accuracy for the ternary LiBs [23] and is defined as follows:

$$U_{\text{OCV}} = f(\text{SOC}) = a_0 + a_1\text{SOC} + \cdots + a_{n-1}\text{SOC}^{n-1} + a_n\text{SOC}^n \tag{7}$$

where $a_0, a_1, \ldots, a_{n-1}, a_n$ are the polynomial coefficients, and n donates the degree of the polynomial. Moreover, in this paper, n is set as 4 by considering both the complexity and fitting accuracy of the algorithm.

As is well known, function fitting can only be carried out when all fitted data have been known, that is, it is impossible to construct the OCV curve in real time. Therefore, in order to model in real time, (7) is converted into a matrix as follows:

$$\begin{cases} \mathbf{\Phi}_k = \left[1, \text{SOC}_k, \cdots, {\text{SOC}_k}^{n-1}, {\text{SOC}_k}^{n}\right] \\ \theta_k = [a_{0,k}, a_{1,k}, \cdots, a_{n-1,k}, a_{n,k}]^T \\ y_k = U_{\text{OCV},k} = \mathbf{\Phi}_k \cdot \theta_k \end{cases} \tag{8}$$

where y_k, $\mathbf{\Phi}_k$, and θ_k are the output vector, data vector, and parameter vector at the kth step, respectively. $U_{\text{OCV},k} = f\,(\text{SOC}_k)$ is the functional relationship of the OCV–SOC curve and can be implemented by the FFRLS algorithm, which is an extension of the RLS algorithm incorporating a forgetting factor λ, which is set to 0.99 in this study. This factor is introduced to overcome the "data saturation" issue and improve the algorithm's tracking capability. The detailed principle and process of FFRLS can be referred to in [29]. This step allows us

to generate the OCV curve online, that is to say, the OCV–SOC functional relationship is modeled in real time.

4.2. SOC Estimation Based on a UKF Algorithm

Next, SOC estimation can be completed by UKF after the OCV curve is constructed. The SOC is defined as the ratio of remaining capacity to available capacity, and its formula is as follows:

$$\mathrm{SOC}_{k+1} = \mathrm{SOC}_k + \frac{\eta i_{\mathrm{t},k} T_s}{Q_a} \tag{9}$$

where SOC_{k+1} and SOC_k are the SOC values estimated at step $k + 1$ and k, respectively; Q_a represents the maximum available capacity of the battery; and η means the Coulomb efficiency. In order to simplify the algorithm, the effects of temperature on Q_a and η are not considered.

According to Figure 1, the discretized state equation and output equation can be written as follows:

$$\begin{bmatrix} u_{1,k+1} \\ u_{2,k+1} \\ \mathrm{SOC}_{k+1} \end{bmatrix} = \begin{bmatrix} e^{-\frac{T_s}{R_{1,k}C_{1,k}}} & 0 & 0 \\ 0 & e^{-\frac{T_s}{R_{2,k}C_{2,k}}} & 0 \\ 0 & 0 & 1 \end{bmatrix} \cdot \begin{bmatrix} u_{1,k} \\ u_{2,k} \\ \mathrm{SOC}_k \end{bmatrix} + \begin{bmatrix} R_{1,k}(1 - e^{-\frac{T_s}{R_{1,k}C_{1,k}}}) \\ R_{2,k}(1 - e^{-\frac{T_s}{R_{2,k}C_{2,k}}}) \\ \frac{\eta T_s}{Q_a} \end{bmatrix} \cdot i_{\mathrm{t},k} \tag{10}$$

$$u_{\mathrm{t},k} = U_{\mathrm{OCV},k} + u_{1,k} + u_{2,k} + R_{0,k} \cdot i_{\mathrm{t},k} \tag{11}$$

where u_1, u_2, and SOC are state variables, and u_t is the output variable. R_0, R_1, and C_1 are the fast dynamic components identified by FMRLS; R_2 and C_2 are the slow dynamic components identified by EKF, which is performed when $\Delta\mathrm{SOC} \geq 0.2\%$; $U_{\mathrm{OCV},k} = f(\mathrm{SOC}_k)$ is from (7).

Equations (10) and (11) can be transformed into the following:

$$\begin{cases} \boldsymbol{X}_{k+1} = \boldsymbol{A}_k \boldsymbol{X}_k + \boldsymbol{B}_k i_{t,k} \\ \boldsymbol{O}_k = \boldsymbol{C}_k \boldsymbol{X}_k + \boldsymbol{D}_k i_{t,k} + f(SOC_k) \end{cases} \tag{12}$$

where the state variable $\boldsymbol{X}_k$ and the output variable $\boldsymbol{O}_k$ are as follows:

$$\boldsymbol{X}_k = [u_{1,k}\ u_{2,k}\ SOC_k]^T \tag{13}$$

$$\boldsymbol{O}_k = u_{\mathrm{t},k} \tag{14}$$

and the coefficient matrices are as follows:

$$\boldsymbol{A}_k = \begin{bmatrix} e^{-\frac{T_s}{R_{1,k}C_{1,k}}} & 0 & 0 \\ 0 & e^{-\frac{T_s}{R_{2,k}C_{2,k}}} & 0 \\ 0 & 0 & 1 \end{bmatrix} \tag{15}$$

$$\boldsymbol{B}_k = \begin{bmatrix} R_{1,k}(1 - e^{-\frac{T_s}{R_{1,k}C_{1,k}}}) & R_{2,k}(1 - e^{-\frac{T_s}{R_{2,k}C_{2,k}}}) & \frac{\eta T_s}{Q_a} \end{bmatrix}^T \tag{16}$$

$$\boldsymbol{C}_k = \begin{bmatrix} 1 & 1 & 0 \end{bmatrix} \tag{17}$$

$$\boldsymbol{D}_k = R_{0,k} \tag{18}$$

SOC can be estimated with (12) using the UKF algorithm. The EKF algorithm linearizes the function by the first-order Taylor series but neglects the second-order and higher-order terms, which causes inevitable linearization errors. Like the EKF, the UKF algorithm is also an extension of the classical KF. Moreover, the UKF involves an unscented transformation before initiating the KF algorithm for nonlinear systems. The unscented transformation offers a high level of approximation precision to achieve second-order Taylor expansion

accuracy and significantly enhances computational precision. The detailed principle and operation of UKF can be found in [30].

5. Results and Discussion

To verify the feasibility and applicability of the algorithm proposed in this paper, a popular experimental dataset published by the Center for Advanced Life Cycle Engineering (CALCE) was utilized for algorithm validation [31]. The CALCE completed various experiments for different batteries. In this paper, the experimental data of the INR18650-20R NCM LiBs, whose electrical characteristics are shown in Table 2, were selected. The incremental current OCV test and mission profile test at three different temperatures (0 °C, 25 °C, and 45 °C) were completed by the CALCE. The mission profile test included four working conditions: dynamic stress test (DST), federal urban driving schedule (FUDS), highway driving schedule (US06), and Beijing dynamic stress test (BJDST). In the mission profile test, the battery is first charged to full capacity using constant current and constant voltage charging and then discharged to 80% SOC after standing alone for a period of time. Next, after standing alone for another period, i.e., 2.6×10^4 s, the current waveform of working conditions is performed on the batteries.

Table 2. Electrical characteristics of INR18650-20R LiBs [31].

Parameters	Values
Rated voltage (V)	3.6
Capacity (mAh)	2000
Maximum/minimum cutoff voltage (V)	4.2/2.5
Maximum current (A)	22
Temperature range (°C)	0–50

5.1. Results of Parameter Identification

Among the four mission profiles tested by the CALCE, DST and FUDS are the most popular used. DST simulates higher dynamic driving conditions, including high speed and significant speed changes, and FUDS simulates urban driving conditions with lower speed. So, these two mission profiles were used for simulation verification in this study. Figures 4 and 5 show the identified parameters of the ECM under FUDS and DST with an initial SOC = 80% at 25 °C. It can be seen that (1) all the parameters identified have similar values and variation tendencies under these two different operating conditions. This overcomes the dilemma presented in many studies, namely that the parameters identified under different working conditions are quite different; (2) there are some fluctuations in the identified results of R_0, R_1, and C_1, which all belong to the FD part and reflect the rapid response of transient current; (3) R_2 and C_2 remain relatively stable because they belong to the SD part and are consistent with the low-frequency diffusion characteristic of lithium-ion batteries. To determine whether the identified parameters have explainable kinetic significance, we performed an analysis as follows:

(1) Ohmic resistance

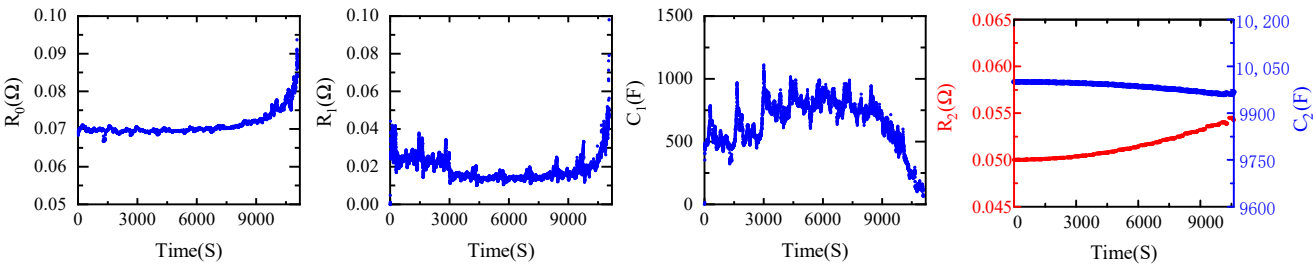

Figure 4. The identified parameters of ECM under FUDS at 25 °C with initial SOC = 80%.

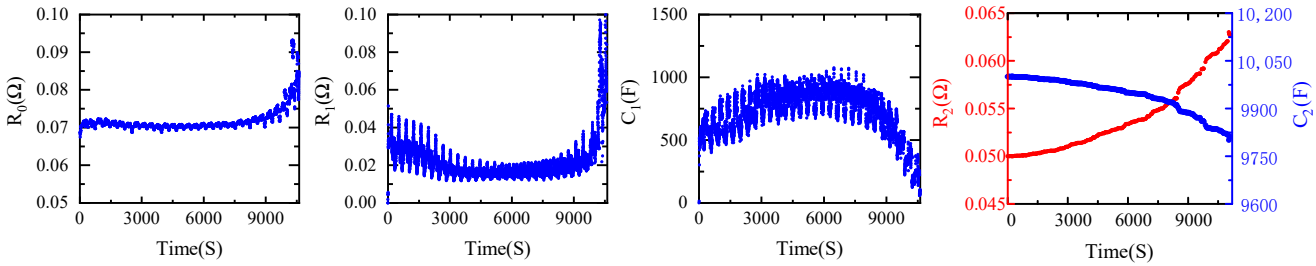

Figure 5. The identified parameters of ECM under DST at 25 °C with initial SOC = 80%.

The overall variation in ohmic resistance R_0 is relatively stable at 0.07 Ω (80% > SOC > 10%), which is consistent with the identified results in [32]. When SOC < 10%, R_0 increases rapidly to around 0.10 Ω, which is consistent with the conclusions drawn by many studies that internal resistance increases with a low SOC [33].

(2) Charge transfer resistance

From Figures 4 and 5, it can be seen that as the SOC decreases, the charge transfer resistance R_1 goes down first and rebounds at the tail. This is because, during the initial discharge stage of the battery, there is an inevitable activation process. As the depth of discharge increases, the battery is activated further, which makes the electrochemical reactions and charge transfer processes easier, so R_1 decreases. As the depth of discharge increases further, the electrolyte active material is consumed contentiously, and the internal structure of the electrode active particles changes, resulting in an increase in the charge transfer resistance [34]. In particular, when the SOC approaches 0, the negative electrode charge transfer resistance increases significantly, leading to a tail-up phenomenon [35]. Reference [36] derived an approximate function of charge transfer resistance from the electrochemical mechanism as follows:

$$Z_{tr} = \frac{\alpha}{\sqrt{\beta_2 SOC^2 + \beta_1 SOC + \beta_0}} \tag{19}$$

where Z_{tr} represents charge transfer resistance; α, β_0, β_1, and β_2 are electrochemical parameters. In addition, the charge transfer resistances in [37,38], which are obtained through the electrochemical impedance spectroscopy experiments, also show the same overall trend as that observed in our study.

(3) Low-frequency Diffusion resistance

The diffusion process of lithium batteries occurs both in the electrode and electrolyte and is driven by the concentration difference in lithium ions. Diffusion in the electrodes is more difficult and slower, so the low-frequency diffusion resistance is mainly the electrode diffusion resistance. As shown in Figures 4 and 5, as the SOC decreases, the diffusion resistance gradually increases. This is due to the decrease in the ion concentration gradient; the diffusion process becomes more difficult according to Fick's law [39].

To further analyze the temperature characteristics of the algorithm, the parameters identified under FUDS at different ambient temperatures are shown in Figure 6, and the results are analyzed as follows: (1) The maximum ohmic resistance R_0 is observed at 0 °C, and the values are similar at 25 °C and 45 °C. The ohmic resistance mainly consists of the resistances of the electrolyte, electrode, membranes, etc. Higher temperatures result in lower electrolyte viscosity and thus lower internal resistance. (2) The charge transfer resistance R_1 and diffusion resistance R_2 both decrease with the increase in temperature because the increased temperature accelerates the speed of ion migration, which reduces the resistance value.

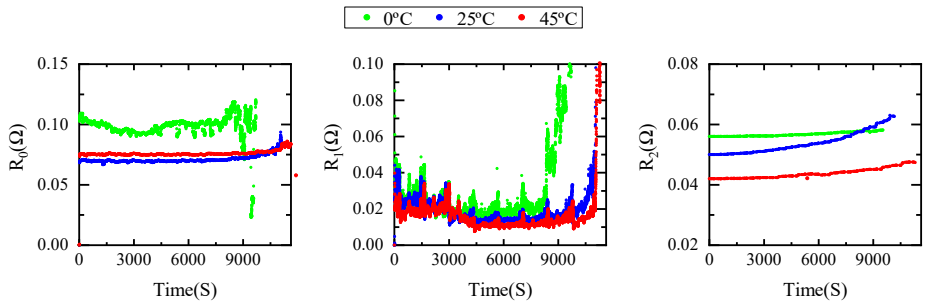

Figure 6. The identified resistances under FUDS with different ambient temperatures.

In summary, the parameters identified using the algorithm proposed in this study have explainable kinetic significance for LiBs. They may benefit the state monitoring of BMS because these parameters are sensitive to battery degradation and SOH.

To verify the accuracy of the identification results, the terminal voltages under FUDS and DST with 80% initial SOC were determined, which are shown in Figure 7, which indicates that the results are in good agreement with the measured values. Root mean square error (RMSE), which is determined using (20), is utilized to evaluate the average deviation between the estimated values $\hat{x}_i$ and the true values x_i.

$$RMSE = \sqrt{\sum_{i=1}^{n} (x_i - \hat{x}_i)^2 / n} \tag{20}$$

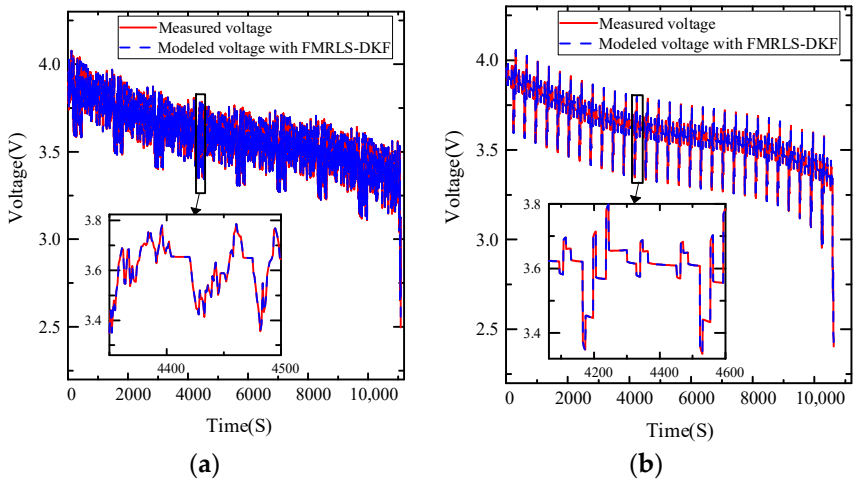

Figure 7. Terminal voltage using the FMRLS-EKF-KF algorithm at 25 °C with (**a**) FUDS and (**b**) DST.

The RMSE of the terminal voltage using the proposed FMRLS-EKF-KF algorithm is shown in Table 3. From this table, it can be seen that the algorithm has high accuracy at various temperatures, and the RMSE is around 1.23 mV at 25 °C.

Table 3. RMSE (mV) of terminal voltage at different ambient temperatures.

Mission Profile	0 °C	25 °C	45 °C
FUDS	5.3	1.52	2.2
DST	4.3	1.23	1.9

5.2. Online OCV Curves

Figure 8 shows the OCV curves constructed online using FUDS and DST at 0 °C, 25 °C, and 45 °C, where the offline data were derived from the offline incremental current tests by the CALCE, and SOC was calculated via standard Ah integral. It can be observed that

without any offline test, the OCV curves constructed online agree with the offline measured data well and have desirable accuracy. Moreover, under different operating conditions and ambient temperatures, the OCV curves all match the offline data well, which also proves that this method has good temperature robustness.

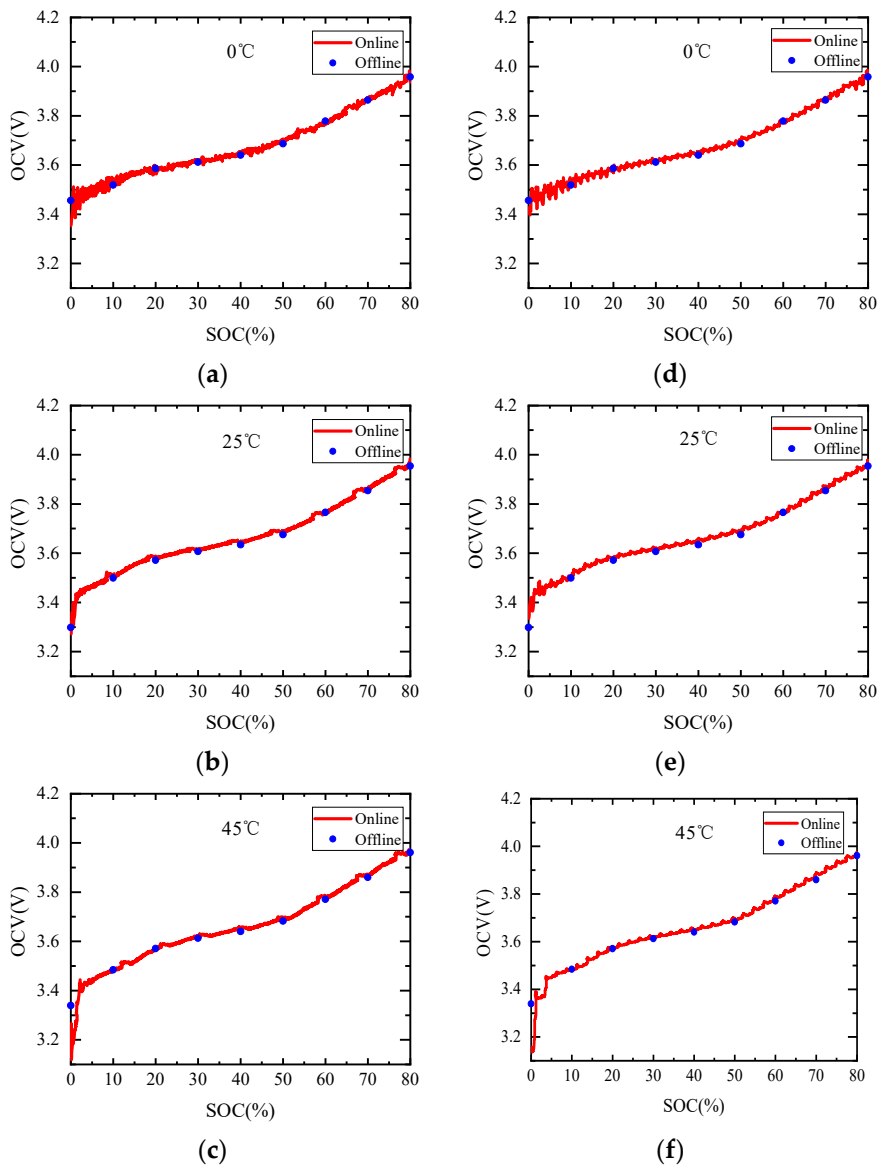

Figure 8. Comparisons of OCV curves obtained from offline and online: (**a**) OCV for FUDS at 0 °C; (**b**) OCV for FUDS at 25 °C; (**c**) OCV for FUDS at 45 °C; (**d**) OCV for DST at 0 °C; (**e**) OCV for DST at 25 °C; (**f**) OCV for DST at 45 °C.

5.3. Results of Estimated SOC

In Figure 9, SOC estimation results using the algorithm proposed in this paper are compared with the results by OCV tests offline, and the SOC reference values are obtained through the ampere–hour integral method. It can be seen that, compared to the offline OCV curve, the SOC estimated in this study has the following characteristics: (1) The SOC estimation errors throughout the process are very small, there is no significant fluctuation, and the estimated SOC is very close to the reference value. (2) The SOC errors of the three temperatures are very close. By contrast, the maximum SOC estimation errors all exceed 1.5% at the initial and final stages using the offline OCV method. In comparison, our method has a satisfied temperature robustness. Furthermore, the RMSE and the maximum

absolute error (Max-AE) are used to quantify the errors in SOC estimations, where the definition of Max-AE is shown as follows:

$$\text{Max-AE} = \max_i |x_i - \hat{x}_i| \tag{21}$$

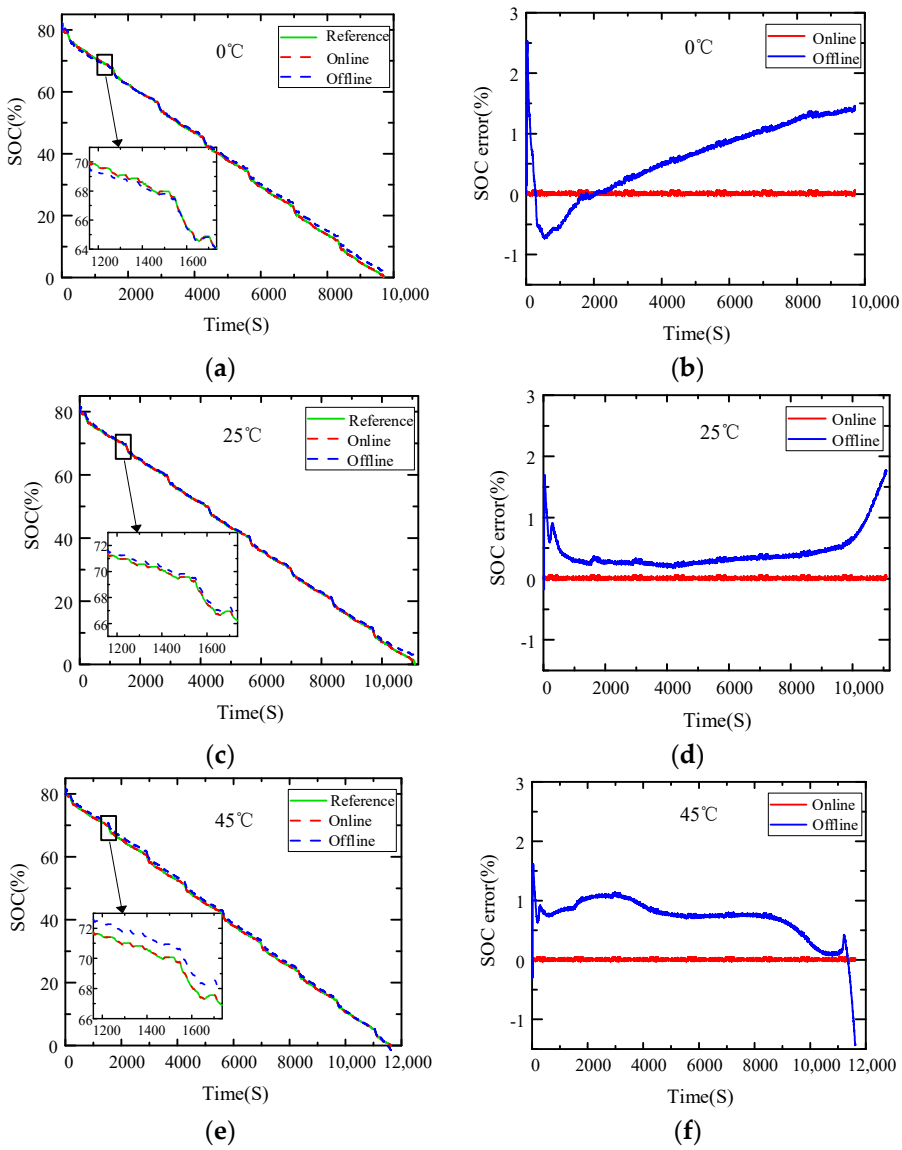

Figure 9. SOC estimation results using FUDS: (**a**) SOC at 0 °C; (**b**) SOC errors at 0 °C; (**c**) SOC at 25 °C; (**d**) SOC errors at 25 °C; (**e**) SOC at 45 °C; (**f**) SOC errors at 45 °C.

The RMSE and Max-AE of SOC estimation using FUDS with the ambient temperatures of 0 °C, 25 °C, and 45 °C are shown in Table 4. From this table, which compares the proposed method with the method using offline OCV test, it can be inferred that the proposed SOC estimation method based on online OCV curve construction is more accurate. For instance, the RMSE is reduced by 30–50 times, and Max-AE is also reduced by 30–40 times. Also, a comparison with the SOC estimation algorithm proposed by Zheng et al. [32] with the same dataset indicates that the RMSE of their study is 0.3585%, but with our method, it is only 0.015%. Meanwhile, comparing our method with the SOC estimation algorithm without offline OCV–SOC tests proposed by Zhang et al. [22], it can be seen that the RMSE of their study is 0.99%; thus, our method has significant advantages.

Table 4. SOC errors at 0 °C, 25 °C, and 45 °C using FUDS.

		0 °C	25 °C	45 °C
RMSE(%)	online	0.020	0.015	0.016
	offline	0.85	0.519	0.782
Max-AE(%)	online	0.065	0.050	0.054
	offline	2.527	1.774	1.616

In summary, compared to SOC estimation using offline OCV tests, the accuracy of the proposed method is greatly improved; the main reasons are as follows: (1) A multi-timescale parameter identification algorithm is presented, where U_{ocv} is independently identified to avoid cross-interference with the low-frequency diffusion process (R_2C_2). Accurate parameters provide assurances for the SOC estimation. (2) SOC feedback is designed in this algorithm, which can correct the online OCV curve in real time to improve the accuracy of SOC further.

6. Conclusions

In order to reduce the influences on SOC estimation by OCV curves obtained via offline tests, an OCV online construction method is presented in this paper. The OCV–SOC relationship was modeled online using a polynomial model and constructed using an FFRLS method. The results show that the algorithm has high accuracy and strong robustness. The major findings and conclusions are as follows: (1) The modified multi-timescale identification algorithm used in this paper can obtain more accurate parameters, which is the first reason for the improved accuracy of SOC estimation. (2) The real-time updating of the OCV–SOC relationship has good applicability for different working conditions and different temperatures. (3) The RMSE values of the SOC estimated at different temperatures and working conditions are around 0.02%, and the Max-AE is less than 0.07%, indicating that the algorithm has high accuracy and strong robustness. Admittedly, the algorithm still has disadvantages, namely (1) the constructed OCV curves have obvious jitters, which should be smoothed to have stable results, and (2) the algorithm is relatively complex and has high computational costs. This issue has not been considered in this paper. In the future, we believe this algorithm should be modified further to reduce complexity and explore its applicability for other types of LiBs.

Author Contributions: Conceptualization, Z.Y.; methodology, X.W. and Z.Y.; software, R.G. and Z.Y.; validation, R.G.; data curation, R.G.; writing—original draft, X.W. and Z.Y.; supervision, X.W.; project administration, X.W.; funding acquisition, L.K. All authors have read and agreed to the published version of the manuscript.

Funding: This research was funded by the Guangdong Provincial Basic and Applied Basic Research Fund, grant number 2022A1515140009.

Data Availability Statement: Data used in this article are publicly available [31].

Conflicts of Interest: The authors declare no conflict of interest.

References

1. Shrivastava, P.; Soon, T.K.; Bin Idris, M.Y.I.; Mekhilef, S. Overview of model-based online state-of-charge estimation using Kalman filter family for lithium-ion batteries. *Renew. Sustain. Energy Rev.* **2019**, *113*, 109233. [CrossRef]
2. Hu, X.S.; Feng, F.; Liu, K.L.; Zhang, L.; Xie, J.L.; Liu, B. State estimation for advanced battery management: Key challenges and future trends. *Renew. Sustain. Energy Rev.* **2019**, *114*, 109334. [CrossRef]
3. Wang, S.L.; Fernandez, C.; Yu, C.M.; Fan, Y.C.; Cao, W.; Stroe, D.I. A novel charged state prediction method of the lithium-ion battery packs based on the composite equivalent modeling and improved splice Kalman filtering algorithm. *J. Power Sources* **2020**, *471*, 228450. [CrossRef]
4. Zhang, S.Z.; Peng, N.; Zhang, X.W. An application-oriented multistate estimation framework of lithium-ion battery used in electric vehicles. *Int. J. Energy Res.* **2021**, *45*, 18554–18576. [CrossRef]
5. Dai, H.F.; Jiang, B.; Hu, X.S.; Lin, X.K.; Wei, X.Z.; Pecht, M. Advanced battery management strategies for a sustainable energy future: Multilayer design concepts and research trends. *Renew. Sustain. Energy Rev.* **2021**, *138*, 110480. [CrossRef]

6. Gu, A.; Zhang, Y.; Wang, X. A Time Series Wasserstein GAN Method for State-of-Charge Estimation of Lithium-Ion Batteries. *J. Power Sources* **2023**, *581*, 233472. [CrossRef]
7. Tian, Y.; Xia, B.Z.; Sun, W.; Xu, Z.H.; Zheng, W.W. A modified model based state of charge estimation of power lithium-ion batteries using unscented Kalman filter. *J. Power Sources* **2014**, *270*, 619–626. [CrossRef]
8. Yang, F.F.; Xing, Y.J.; Wang, D.; Tsui, K.L. A comparative study of three model-based algorithms for estimating state-of-charge of lithium-ion batteries under a new combined dynamic loading profile. *Appl. Energy* **2016**, *164*, 387–399. [CrossRef]
9. Lin, Q.Z.; Li, X.Q.; Tu, B.C.; Cao, J.W.; Zhang, M.; Xiang, J.W. Stable and Accurate Estimation of SOC Using eXogenous Kalman Filter for Lithium-Ion Batteries. *Sensors* **2023**, *23*, 467. [CrossRef]
10. Guo, J.S.; Liu, S.L.; Zhu, R. An unscented kalman filtering method for estimation of state-of-charge of lithium-ion battery. *Front. Energy Res.* **2023**, *10*, 998002. [CrossRef]
11. Xiao, L.Z.; Li, X.N.; Jiang, Q.Y.; Geng, G.C. Online state-of-charge estimation refining method for battery energy storage system using historical operating data. *J. Energy Storage* **2023**, *57*, 106262. [CrossRef]
12. Zheng, Y.J.; Ouyang, M.G.; Han, X.B.; Lu, L.G.; Li, J.Q. Investigating the error sources of the online state of charge estimation methods for lithium-ion batteries in electric vehicles. *J. Power Sources* **2018**, *377*, 161–188. [CrossRef]
13. Xiong, R.; Yu, Q.Q.; Wang, L.Y.; Lin, C. A novel method to obtain the open circuit voltage for the state of charge of lithium-ion batteries in electric vehicles by using H infinity filter. *Appl. Energy* **2017**, *207*, 346–353. [CrossRef]
14. Xu, X.; Xu, Z.; Wang, T.S.; Xu, J.N.; Pei, L. Open-circuit voltage curve reconstruction for degrading lithium-ion batteries utilizing discrete curve fragments from an online dataset. *J. Energy Storage* **2022**, *56*, 106003. [CrossRef]
15. Fernando, A.; Kuipers, M.; Angenendt, G.; Kairies, K.-P.; Dubarry, M. Benchmark dataset for the study of the relaxation of commercial NMC-811 and LFP cells. *Cell Rep. Phys. Sci.* **2024**, *5*, 101754. [CrossRef]
16. Campestrini, C.; Kosch, S.; Jossen, A. Influence of change in open circuit voltage on the state of charge estimation with an extended Kalman filter. *J. Energy Storage* **2017**, *12*, 149–156. [CrossRef]
17. Yang, X.-G.; Liu, T.; Gao, Y.; Ge, S.; Leng, Y.; Wang, D.; Wang, C.-Y. Asymmetric Temperature Modulation for Extreme Fast Charging of Lithium-Ion Batteries. *Joule* **2019**, *3*, 3002–3020. [CrossRef]
18. Pei, L.; Wang, T.S.; Lu, R.G.; Zhu, C.B. Development of a voltage relaxation model for rapid open-circuit voltage prediction in lithium-ion batteries. *J. Power Sources* **2014**, *253*, 412–418. [CrossRef]
19. Zhou, M.Y.; Zhang, J.B.; Ko, C.J.; Chen, K.C. Precise prediction of open circuit voltage of lithium-ion batteries in a short time period. *J. Power Sources* **2023**, *553*, 232295. [CrossRef]
20. Yang, J.F.; Huang, W.X.; Xia, B.; Mi, C. The improved open-circuit voltage characterization test using active polarization voltage reduction method. *Appl. Energy* **2019**, *237*, 682–694. [CrossRef]
21. Ko, C.-J.; Chen, K.-C. Using Tens of Seconds of Relaxation Voltage to Estimate Open Circuit Voltage and State of Health of lithium ion Batteries. *Appl. Energy* **2024**, *357*, 122488. [CrossRef]
22. Zhang, S.Z.; Zhang, X.W. A novel non-experiment-based reconstruction method for the relationship between open-circuit-voltage and state-of-charge/state-of-energy of lithium-ion battery. *Electrochim. Acta* **2022**, *403*, 139637. [CrossRef]
23. Wang, L.; Sun, J.; Cai, Y.; Lian, Y.; Jin, M.; Zhao, X.; Wang, R.; Chen, L.; Chen, J. A novel OCV curve reconstruction and update method of lithium-ion batteries at different temperatures based on cloud data. *Energy* **2023**, *268*, 126773. [CrossRef]
24. Chen, X.K.; Lei, H.; Xiong, R.; Shen, W.X.; Yang, R.X. A novel approach to reconstruct open circuit voltage for state of charge estimation of lithium ion batteries in electric vehicles. *Appl. Energy* **2019**, *255*, 113758. [CrossRef]
25. Yang, Z.; Wang, X. An improved parameter identification method considering multi-timescale characteristics of lithium-ion batteries. *J. Energy Storage* **2023**, *59*, 106462. [CrossRef]
26. Kalman, R.E. A New Approach to Linear Filtering and Prediction Problems. *J. Basic Eng.* **1960**, *82*, 35–45. [CrossRef]
27. Bucy, R.S.; Senne, K.D. Digital synthesis of non-linear filters. *Automatica* **1971**, *7*, 287–298. [CrossRef]
28. Dai, H.F.; Xu, T.J.; Zhu, L.T.; Wei, X.Z.; Sun, Z.C. Adaptive model parameter identification for large capacity Li-ion batteries on separated time scales. *Appl. Energy* **2016**, *184*, 119–131. [CrossRef]
29. Xia, B.; Lao, Z.; Zhang, R.; Zhang, R.; Tian, Y.; Chen, G.; Sun, Z.; Wang, W.; Sun, W.; Lai, Y.; et al. Online Parameter Identification and State of Charge Estimation of Lithium-Ion Batteries Based on Forgetting Factor Recursive Least Squares and Nonlinear Kalman Filter. *Energies* **2018**, *11*, 3. [CrossRef]
30. Julier, S.; Uhlmann, J.; Durrant-Whyte, H.F. A new method for the nonlinear transformation of means and covariances in filters and estimators. *IEEE Trans. Autom. Control* **2000**, *45*, 477–482. [CrossRef]
31. Center for Advanced Life Cycle Engineering. Battery Research Data. Available online: https://calce.umd.edu/data (accessed on 2 December 2015).
32. Zheng, F.D.; Xing, Y.J.; Jiang, J.C.; Sun, B.X.; Kim, J.; Pecht, M. Influence of different open circuit voltage tests on state of charge online estimation for lithium-ion batteries. *Appl. Energy* **2016**, *183*, 513–525. [CrossRef]
33. Fotouhi, A.; Auger, D.J.; Propp, K.; Longo, S. Accuracy Versus Simplicity in Online Battery Model Identification. *IEEE Trans. Syst. Man Cybern. Syst.* **2018**, *48*, 195–206. [CrossRef]
34. Feng, F.; Yang, R.; Meng, J.; Xie, Y.; Zhang, Z.; Chai, Y.; Mou, L. Electrochemical impedance characteristics at various conditions for commercial solid-liquid electrolyte lithium-ion batteries: Part 1. experiment investigation and regression analysis. *Energy* **2022**, *242*, 122880. [CrossRef]

35. Huang, J.; Li, Z.; Zhang, J.B. Dynamic electrochemical impedance spectroscopy reconstructed from continuous impedance measurement of single frequency during charging/discharging. *J. Power Sources* **2015**, *273*, 1098–1102. [CrossRef]
36. Wang, X.Y.; Li, J.; Chen, S.; Zhang, G.; Jiang, B.; Wei, X.; Dai, H. Online Detection of Lithium Plating Onset for Lithium-Ion Batteries Based on Impedance Changing Trend Identification During Charging Processes. *IEEE Trans. Transport. Electrific.* **2023**, *9*, 3487–3497. [CrossRef]
37. Tran, M.K.; Mathew, M.; Janhunen, S.; Panchal, S.; Raahemifar, K.; Fraser, R.; Fowler, M. A comprehensive equivalent circuit model for lithium-ion batteries, incorporating the effects of state of health, state of charge, and temperature on model parameters. *J. Energy Storage* **2021**, *43*, 103252. [CrossRef]
38. Ruan, H.J.; Ruan, H.; Sun, B.; Jiang, J.; Zhang, W.; He, X.; Su, X.; Bian, J.; Gao, W. A modified-electrochemical impedance spectroscopy-based multi-time-scale fractional-order model for lithium-ion batteries. *Electrochim. Acta* **2021**, *394*, 139066. [CrossRef]
39. Wang, Q.K.; He, Y.J.; Shen, J.N.; Hu, X.S.; Ma, Z.F. State of Charge-Dependent Polynomial Equivalent Circuit Modeling for Electrochemical Impedance Spectroscopy of Lithium-Ion Batteries. *IEEE Trans. Power Electron.* **2018**, *33*, 8449–8460. [CrossRef]

Disclaimer/Publisher's Note: The statements, opinions and data contained in all publications are solely those of the individual author(s) and contributor(s) and not of MDPI and/or the editor(s). MDPI and/or the editor(s) disclaim responsibility for any injury to people or property resulting from any ideas, methods, instructions or products referred to in the content.